

OccGaussian: 3D Gaussian Splatting for Occluded Human Rendering

Jingrui Ye
Tsinghua Shenzhen International
Graduate School, Tsinghua University
Shenzhen, China
yjr22@mails.tsinghua.edu.cn

Zhongkai Zhang
Tsinghua Shenzhen International
Graduate School, Tsinghua University
Shenzhen, China
zzk21@mails.tsinghua.edu.cn

Yujiao Jiang
Tsinghua Shenzhen International
Graduate School, Tsinghua University
Shenzhen, China
jiangyj20@mails.tsinghua.edu.cn

Qingmin Liao*
Tsinghua Shenzhen International
Graduate School, Tsinghua University
Shenzhen, China
liaoqm@tsinghua.edu.cn

Wenming Yang
Tsinghua Shenzhen International
Graduate School, Tsinghua University
Shenzhen, China
yang.wenming@sz.tsinghua.edu.cn

Zongqing Lu
Tsinghua Shenzhen International
Graduate School, Tsinghua University
Shenzhen, China
luzq@sz.tsinghua.edu.cn

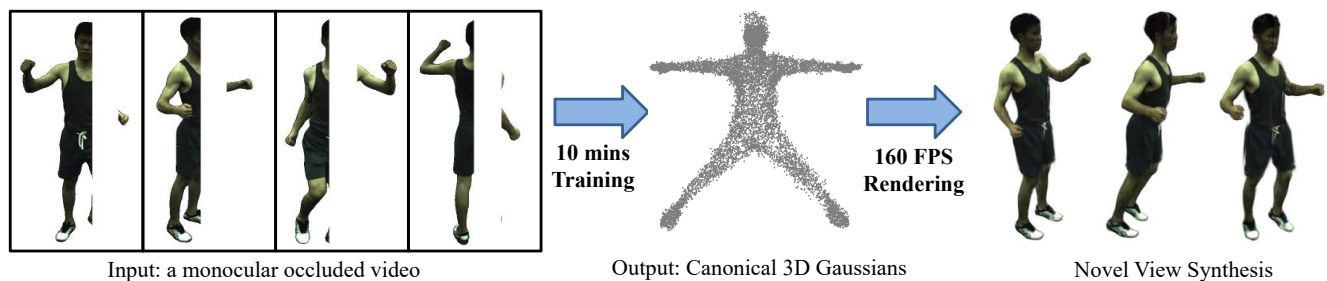


Figure 1. Overview of OccGaussian. We develop an efficient method for rendering human under severe occlusions with the help of 3D Gaussian Splatting [19]. Given a real-world monocular sequence of dynamic human with a tracked skeleton and foreground masks, our method trains within 6 minutes on a single GPU and supports rendering up to 160 FPS. Meanwhile OccGaussian achieves comparable or better rendering quality against the state-of-the-art method [55] that needs to train over one day, and takes several seconds to render a single image.

Abstract

Rendering dynamic 3D humans from monocular videos is crucial for various applications such as virtual reality and digital entertainment. Most methods assume the human is in an unobstructed scene, while various objects may cause the occlusion of body parts in real-life scenarios. Previous method utilizing NeRF for surface rendering to recover the

occluded areas, but it requiring more than one day to train and several seconds to render, failing to meet the requirements of real-time interactive applications. To address these issues, we propose **OccGaussian** based on 3D Gaussian Splatting, which can be trained within 6 minutes and produces high-quality human renderings up to 160 FPS with occluded input. OccGaussian initializes 3D Gaussian distributions in the canonical space, and we perform occlusion feature query at occluded regions, the aggregated pixel-align feature is extracted to compensate for the missing information. Then we use Gaussian Feature MLP to further process the feature along with the occlusion-aware loss functions to better perceive the occluded area. Extensive experiments both in simulated and real-world occlusions, demonstrate that our method achieves comparable or even superior performance compared to the state-of-the-art method. And we improving training and inference speeds by 250x and 800x, respectively. Our code will be available for research purposes.

CCS Concepts: • Computing methodologies → Rendering.

*Corresponding author.

Permission to make digital or hard copies of all or part of this work for personal or classroom use is granted without fee provided that copies are not made or distributed for profit or commercial advantage and that copies bear this notice and the full citation on the first page. Copyrights for components of this work owned by others than the author(s) must be honored. Abstracting with credit is permitted. To copy otherwise, or republish, to post on servers or to redistribute to lists, requires prior specific permission and/or a fee. Request permissions from permissions@acm.org.
MM '24, 28 October - 1 November 2024, Melbourne, Australia

© 2018 Copyright held by the owner/author(s). Publication rights licensed to ACM.

ACM ISBN 978-1-4503-XXXX-X/18/06

<https://doi.org/XXXXXXX.XXXXXXX>

Keywords: human modeling, rendering under occlusion, 3D Gaussian Splatting

ACM Reference Format:

Jingrui Ye, Zhongkai Zhang, Yujiao Jiang, Qingmin Liao, Wenming Yang, and Zongqing Lu. 2018. OccGaussian: 3D Gaussian Splatting for Occluded Human Rendering. In *Proceedings of Proceedings of the 32th ACM International Conference on Multimedia (MM '24)*. ACM, New York, NY, USA, 16 pages. <https://doi.org/XXXXXXX.XXXXXXX>

1 Introduction

For a long time, rendering high-quality humans has played an important role in industries such as movies, games, and entertainment, and its modeling effect directly affects people’s visual experience. Due to the intricate topology of the human body, how to reconstruct realistic humans in real-life scenarios is still a formidable challenge.

With the emergence of NeRF and its variants [3, 8, 31, 33, 67], progress in human rendering has been increasingly rapid, many methods are now capable of rendering photo-realistic human [34, 51, 59, 64]. The datasets used by these methods are all captured in ideal laboratory environments, where all parts of the human are free from occlusion in spacious scenes. However, in real-world scenarios, it is not guaranteed that the scenes are entirely unobstructed during capture; various objects may exist, leading to certain occluded parts of the human body. Training with these occluded images will seriously degrade the rendering quality of these methods. Moreover, laboratory environments allow us to capture dense, synchronized multi-view data, but this is difficult to achieve in real-life scenes, where we can only capture from a single view. Due to the lack of ground truth in occluded regions and the limited information from only one view, previous methods fail to handle the occluded data.

Addressing the drawbacks mentioned above, OccNeRF [55] stands out as the first dynamic human rendering method for occluded environments. It introduces a surface-based rendering strategy, replacing points with sub-regions of sampled points to achieve better adjustments in occluded regions. Although OccNeRF has achieved decent rendering results in occluded areas, considering the inherent limitations of NeRF, which requires hundreds of forward predictions of MLP for each pixel during rendering. So OccNeRF needs at least one day of training with high demands on GPU memory. And like NeRF, OccNeRF also needs a large MLP for inference, resulting in slow rendering. These shortcomings restrict the application of OccNeRF in real-world scenarios.

Point-based rendering has emerged as an effective alternative to NeRFs [42, 45, 57, 72]. With the recently proposed 3D Gaussian Splatting (3DGS) model [19], training takes only a few minutes; rendering speeds are tens of times faster than the best NeRF method [33], and achieve state-of-the-art rendering quality for static scenes. Subsequent works [13, 15, 39, 40] applying 3DGS to human rendering have

also demonstrated that compared to NeRF, 3DGS can render more quickly with shorter training time while maintaining competitive rendering performance.

To address the slow training and rendering of OccNeRF, we propose OccGaussian to render occluded human in monocular videos. Leveraging the capabilities of 3DGS, our approach significantly reduces the time for training and rendering, decreases memory consumption, and improves rendering quality. We propose the aggregated pixel-align features from K-nearest visible points to substitute occluded points, thus better utilizing the local information to compensate for the lack of ground truth in occluded regions. Meanwhile, we update the weights of each point, allowing features from highly visible areas to be more dominant. Finally, since conventional losses used in human rendering tasks are ineffective in occluded settings, we design occlusion loss and consistency loss to encourage the network not to remove occluded points excessively, resulting in a more complete rendering result.

Our experiments show that, in the single-view occluded human rendering task, compare to the state-of-the-art method OccNeRF [55], OccGaussian can train in minutes, which is 250 times faster than OccNeRF, and the rendering speed up to 160 FPS is improved by 800 times. Our method maintains comparable rendering quality and even outperforms OccNeRF. In summary, our work contributes in the following aspects:

1. We propose OccGaussian, which, to the best of our knowledge, is the first work that applies 3DGS to render human in occlusion scenarios. It enables rapid training (6~13 minutes) and real-time rendering (up to 169 FPS), making it more convenient for real-time applications.
2. We propose a K-nearest feature query in occluded regions, combined with an aggregated pixel-align feature. And we design occlusion loss and consistency loss, help us to render appropriate textures in occluded regions.
3. Experiments on two datasets fully demonstrate that OccGaussian achieves SOTA occluded human rendering quality while ensuring rapid training and real-time rendering.

2 Related Works

Point-Based Rendering and Neural Radiance Field. Point sampling in geometric rendering has always been an indispensable part. This book [10] provides a detailed overview of traditional point cloud rendering algorithms. Recently, there has been an increasing focus on differentiable rendering based on points. DSS [63] projects point cloud onto a 3D grid and generates differentiable surface patches at the projected positions. NPBG [1] introduces a multi-scale rendering strategy to render point clouds at different resolutions.

NeRF [31] pioneered the neural radiance field, combining them with volumetric rendering to obtain the color of pixels by aggregating sampled points along rays. Subsequent works [2, 3, 8, 67] continuously improve the rendering quality and training/inference speed of NeRF. 3DGS [19] has recently emerged as a transformative approach in point-based rendering, leveraging Gaussian ellipsoid space to balance better rendering efficiency and quality.

Human avatar rendering. NeRF is initially proposed for rendering the static scene, which implicitly models it with a neural network. Based on parametric models of human [25, 28, 36], numerous works have applying NeRF to dynamic human rendering [4, 5, 22, 30, 37, 38, 49, 52, 59, 64, 71]. In these works, Transhuman [34] introduced Transformer [47] to capture global relationships between body parts. SHERF [14] can train on a single image and reconstruct an animatable 3D human. UV volumes [7] leveraging pre-defined UV human maps and sparse 3D convolutions for feature encoding, which accelerated rendering but didn't shorten training time. And some methods [9, 17] applying a variant of NeRF [33] aim to accelerate training and inference, but with poorer generalization. With the advent of 3D Gaussian Splatting [19], many works have migrated it to human rendering [13, 15, 18, 21, 23, 24, 26, 32, 35, 39, 40, 58, 65, 70], significantly improving training/inference speed and rendering quality compared to NeRF-based methods. However, all these methods can only trained on data captured in ideal environments without occlusions, where all parts of a person are clearly visible. In contrast, the data used in our work are occluded images of humans from a single view, with the aim of getting complete and high-quality rendering results for better application in real-world scenarios.

Occluded Human Reconstruction. Prior works primarily focused on pose estimation or human reconstruction for occluded humans. DensePose [11] introduced convolution networks to learn the mapping from 2D image to 3D human surface, processing dense coordinates at multiple frames per second to achieve dynamic pose estimation. Recent works [16, 27, 44, 48, 60, 66, 73] have shown improved performance in estimating human poses under occlusions, exhibiting robustness even in outdoor scenes.

However, the works above reconstruct parametric models of humans, only representing rough body shapes and poses, unable to recover clothing details or even facial expressions. To address this, sun et al. [46] use sparse-view sequences as input, and employ a layer-by-layer scene decoupling strategy for the reconstruction and rendering of people and objects. Xiang et al. [55] proposed OccNeRF, which combines surface-based rendering with visibility attention to render occluded humans. It can partially recover occluded regions, but OccNeRF still inherits NeRF's drawbacks, being too slow during training and inference and requiring significant GPU memory due to its ray sampling approach. Wild2Avatar [54] is

also a neural occluded human rendering method. It introduces an occlusion-aware scene parameterization method that decomposes the scene into: occlusion, human body, and background. However, Wild2Avatar still employs NeRF for rendering and it's unable to circumvent the slow training and inference issue.

3 Methods

In this section, we start by briefly reviewing the linear blend skinning (LBS) function and 3D Gaussian Splatting [19] in section 3.1, we then present OccGaussian by introducing 3D Gaussian Forward Skinning (section 3.2), Occlusion Feature Query (section 3.3), Gaussian Feature MLP (section 3.4), and our novel loss function (section 3.5) to archive high rendering quality as well as fast training/inference under occlusions. An overview of OccGaussian is shown in Figure 2.

3.1 Preliminary

Parametric model of human. Parametric human models [28, 36, 41, 56] describe human shape and pose using a set of parameters, enabling modeling, animation and rendering. The most widely used model is the SMPL [28] model. SMPL defines shape parameters $\beta \in \mathbb{R}^{10}$ and pose parameters $\theta \in \mathbb{R}^{10}$, use the function $M(\beta, \theta)$ to output $N = 6980$ vertices of mesh. The Linear Blend Skinning (LBS) algorithm is used to transform the SMPL vertices x^c from canonical space to points x^p in posed space:

$$x^p = \sum_{k=1}^K \omega_k (G_k(J, \theta)) x^c + b_k(J, \theta, \beta) \quad (1)$$

where J represents the positions of K joints, ω_k represents the skinning weights of the k -th joint to the SMPL vertex, $G_k(\cdot)$ and $b_k(\cdot)$ denote the transformation matrix and translation vector of joint k , respectively.

3D Gaussian Splatting [19]. NeRF [31] represents the scene using a 5D neural radiance field and then computes pixel color and opacity through volume rendering. In contrast to NeRF, 3DGS employs unstructured, explicit 3D Gaussian distributions to represent the scene, which is differentiable and easy to project. 3DGS models the geometry as a set of 3D Gaussian functions that do not require normal, the Gaussian sphere is defined by covariance matrix Σ in world space, with its mean μ as the center:

$$G(x) = \frac{1}{(2\pi)^{\frac{3}{2}} |\Sigma|^{\frac{1}{2}}} e^{-\frac{1}{2}(x-\mu)^T \Sigma^{-1} (x-\mu)} \quad (2)$$

And we need to project points onto the image plane for rendering, given a transformation matrix W from world coordinates to camera coordinates, the covariance matrix Σ' in camera coordinates is computed as: $\Sigma' = JW\Sigma W^T J^T$, where J is the Jacobian matrix of the affine transformation for projection. Since the covariance matrix needs to be positive semi-definite, 3DGS represents Σ by the scaling matrix S and rotation matrix R : $\Sigma = RSS^T R^T$, they are respectively stored as the scaling vector $s \in \mathbb{R}^3$ and rotation quaternion $q \in \mathbb{R}^4$.

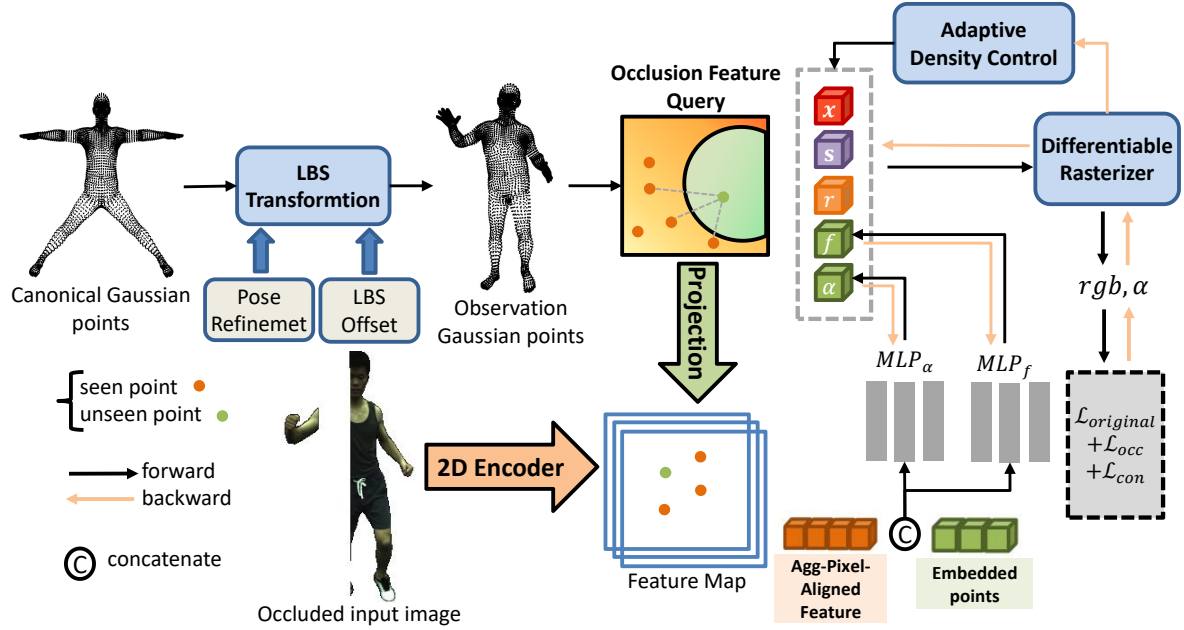


Figure 2. OccGaussian Framework. We initialize 3D Gaussian distributions in the canonical space, then transform the points from canonical space to pose space through linear blend skinning according to the SMPL parameters. Meanwhile, the input image is encoded to obtain feature maps, and then we project points onto the 2D image plane and perform feature query in the occluded regions, extracting aggregated pixel-aligned features for each occluded point. We concatenate this feature with the embedded occluded point and put them into MLP to predict the spherical harmonic coefficients f and the opacity α . Following 3DGS [19], we apply the tile-based differentiable rasterizer to achieve fast rendering and adaptive density control during training. Despite the standard loss functions, we also design occlusion loss and consistency loss to prevent the model from learning background information in occluded regions.

With these formulas, we can transform the 3D points from world coordinates to ray coordinates:

$$G(x) = \frac{1}{(2\pi)^{\frac{3}{2}} |\Sigma'|^{\frac{1}{2}}} e^{-\frac{1}{2}(x-\mu')^T \Sigma'^{-1} (x-\mu')} \quad (3)$$

where $\mu' = c(W\mu + t)$, $c(\cdot)$ denotes the projection function, and t is the translation vector. After projection, we compute the number of overlapping Gaussians at each pixel, as well as the color c_i and opacity α_i of all points at that pixel, and sort them by depth. Finally, blending the N-ordered Gaussians to obtain the pixel color:

$$\hat{C} = \sum_{i=0}^N c_i \alpha_i \prod_{j=1}^{i-1} (1 - \alpha_j) \quad (4)$$

3DGS initializes Gaussian distributions with sparse point clouds from SfM [43], and the color of each point is represented by spherical harmonic coefficients (Shs). 3DGS also proposes adaptive density control, it clones points with large gradients and small scaling matrices and splits points with large gradients and large scaling matrices. And after every 100 iterations, points with opacities below a threshold are pruned.

3.2 3D Gaussian Forward Skinning

3DGS and its variants [19, 29, 53, 61] achieve fast rendering of static or dynamic scenes by splatting a set of 3D Gaussian points. Following Gauhuman [15], we can similarly represent the human with Gaussian distributions in canonical space, and map the points to pose space of each frame using LBS transformation. Due to the favorable properties of 3D Gaussians, such as rotational invariance, we can directly rotate and translate the mean and covariance matrices of each point:

$$\begin{aligned} x^p &= G(J^p, \theta^p) x^c + b(J^p, \theta^p, \beta^p) \\ \Sigma^p &= G(J^p, \theta^p) \Sigma^c G(J^p, \theta^p)^T, \end{aligned} \quad (5)$$

where x^p , Σ^p , x^c , and Σ^c are the mean and covariance matrix of points in canonical and posed space respectively. And $G(J^p, \theta^p) = \sum_{k=1}^K w_k G_k(J^p, \theta^p)$ is the rotation matrix, $b(J^p, \theta^p, \beta^p) = \sum_{k=1}^K w_k b_k(J^p, \theta^p, \beta^p)$ is the translation vector, where K is the joint number. $G_k(J^p, \theta^p)$ and $b_k(J^p, \theta^p, \beta^p)$ are the transformation matrix and translation vector of joint k respectively, w_k is the LBS weight.

LBS Weight Field and Pose Refinement. We employ $\text{MLP}_{\Phi_{\text{lbs}}}(\cdot)$ to predict LBS weight offset for each SMPL vertex following Gauhuman [15]. For each point, we find its nearest SMPL vertex with weight w_k^{SMPL} , and add the predicted offset

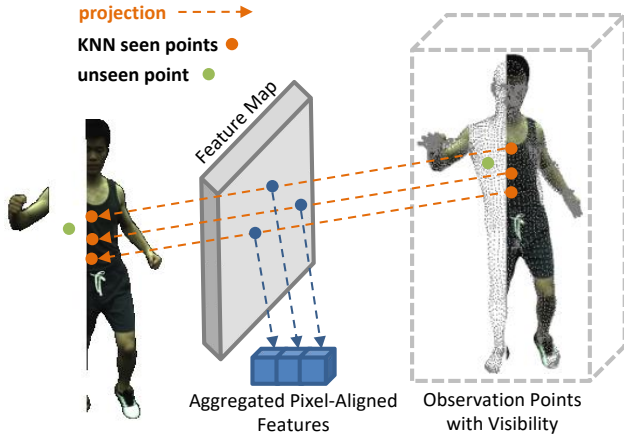


Figure 3. Occlusion Feature Query. For each occluded point (green point), we first query its K-nearest visible points (orange point) among all visible points, and then project these K-nearest visible points onto the feature maps to extract pixel-aligned features.

$\text{MLP}_{\Phi_{\text{lbs}}}(\gamma(x^c))$:

$$w_k = \frac{e^{\log(w_k^{\text{SMPL}} + 10^{-8}) + \text{MLP}_{\Phi_{\text{lbs}}}(\gamma(x^c))[k]}}{\sum_{k=1}^K e^{\log(w_k^{\text{SMPL}} + 10^{-8}) + \text{MLP}_{\Phi_{\text{lbs}}}(\gamma(x^c))[k]}} \quad (6)$$

where $\gamma(\cdot)$ is position encoding. For the body pose θ , we also introduced pose refinement form Gauhuman [15], add a $\text{MLP}_{\Phi_{\text{pose}}}(\cdot)$ to correct SMPL pose θ^{SMPL} :

$$\theta = \theta^{\text{SMPL}} \otimes \text{MLP}_{\Phi_{\text{pose}}}(\theta), \quad (7)$$

With the LBS offset and pose refinement modules, our SMPL parameters can be more accurate which leads to better rendering results. Previous works [6, 17, 51, 62] have also demonstrated the effectiveness. After training, the canonical points along with the transform matrix $\{R_{i=1}^N\}$ and translations vectors $\{T_{i=1}^N\}$ will be saved for inference, where N is the number of views. During inference the points x^c can be easily transform to posed space x^o at view i : $x^o = R_i x^c + T_i$, which further increases the rendering.

3.3 Occlusion Feature Query

Motivation. Although previous human rendering methods based on NeRF or 3DGS have achieved great rendering quality in non-occluded environments, their performance significantly deteriorates under even slight occlusion. For 3DGS, if we directly apply it to render occluded humans, it will completely fail to recover the occluded regions. As 3DGS is based on point rendering, and points are independent of each other, if a point is under occlusion, there is no ground truth supervision for it. These occluded points will be treated as blank background areas during training, resulting in their opacity being close to zero. During adaptive density control, the opacity of these points is below the threshold and therefore being pruned. Even if these points are not pruned,

their spherical harmonic coefficients still represent blank information that cannot contribute to rendering.

K-nearest Occluded Points Query. To solve this problem, we draw inspiration from the traditional image inpainting method, utilizing the redundancy inherent in the image by using the information from known parts to predict the occluded regions. Considering the prior that the human body structure and the clothing texture are most similar in nearby regions, we decide to fill the occluded regions using information from the nearest non-occluded parts. Firstly, Using the provided camera parameters, we can project the 3D points after LBS transformation $x \in \mathbb{R}^{N \times 3}$ onto the 2D image plane and determine their visibility based on whether they lie within the foreground mask α_{fg} or not. This will give us N_1 visible points $x_{seen} \in \mathbb{R}^{N_1 \times 3}$ and N_2 occluded points $x_{occ} \in \mathbb{R}^{N_2 \times 3}$, where $N = N_1 + N_2$. We can easily find that the occluded points lack ground truth, so similar to the principles of image inpainting, we will replace these blank points with information from their nearest visible points. Specifically, for each occluded point, we query its K-nearest neighbors among all visible points x_{seen} , so we can get $N_2 \times K$ points denoted as $x_{knn} \in \mathbb{R}^{N_2 \times K \times 3}$, where K is the number of nearest visible points. After experiments, we choose the hyperparameter $K = 3$ here.

Aggregated Pixel-Aligned Feature. At the same time, we encode the input image $I \in \mathbb{R}^{H \times W \times 3}$ using a deep convolution encoder Φ to obtain the feature maps $I_{fea} \in \mathbb{R}^{H \times W \times C}$, where C is the channel dimension. Similar to the approach in [14, 30, 69], We project the K-nearest points $x_{knn} \in \mathbb{R}^{N_2 \times K \times 3}$ onto each feature planes, and bi-linearly interpolate the grid values to extract the pixel-aligned features for each point, denote as $h \in \mathbb{R}^{N_2 \times K \times C}$. The pixel-aligned features help better incorporate the local texture information from 2D images into 3D points. The above processes to extract feature can be formulated as:

$$h = \Gamma(\Pi(I_{fea}; x_{knn})) \quad (8)$$

Where $\Pi(\cdot)$ denotes the 3D-to-2D projection, and $\Gamma(\cdot)$ is the bilinear interpolation. Figure 3 illustrates the process above.

However, some of the K-nearest visible points may have been occluded in previous frames for a long time, reducing their credibility seriously. Following OccNeRF [55], we propose occlusion-aware aggregation to refine the K-nearest features. We define a visibility weights $\rho \in \mathbb{R}^{N \times 1}$ on the canonical SMPL vertices. During training, if a point is visible, the corresponding weight is incremented by 1, then we can weight the features of K-nearest visible points h , obtaining $h_{agg} \in \mathbb{R}^{N_2 \times C}$:

$$h_{agg} = \sum_{i=1}^K \rho_i h_i, \quad (9)$$

Note that our visibility weights will no longer update after the adaptive density control begins.

3.4 Gaussian Feature MLP

Previous work [53, 61] following the approach of 3DGS [19], learning the viewpoint-dependent colors by storing features within each 3D Gaussian. The stored color feature f consists of a set of orthogonal spherical harmonic coefficients, where the color at each point is computed through the dot product of spherical harmonic basis functions and the view direction:

$$c = (\gamma(d), f) \quad (10)$$

Here, d represents the view direction, i.e., the direction from the 3D Gaussian towards the camera center. And γ denotes the spherical harmonic basis function. While this approach is straightforward and efficient for 3DGS to render static scenes, we find it unsuitable for occluded regions. As our input is a monocular video, the view direction in world space is sole and fixed, leading to poor generalization of our model to unseen test views. Additionally, directly replacing occluded points with information from nearest neighbors, though simple, is too reliant on local information. Therefore, we add multi-layer perceptrons(MLP) to further model the colors of occluded regions. Since the positional information of occluded regions, i.e., mean and covariance, will not be affected by occlusion, we only employ MLP to learn the spherical harmonic coefficients f and opacity α for occluded points. Specifically, with the aforementioned aggregated pixel-aligned feature $h_{agg} \in \mathbb{R}^{N_2 \times C}$, we concatenate the fused features with the embedded occluded 3D points x_{occ} , and finally put them into MLP_{shs} and $MLP_{opacity}$ to predict the spherical harmonic coefficients $f_{occ} \in \mathbb{R}^{3 \times 16}$ and opacity $\alpha_{occ} \in \mathbb{R}^1$ for each occluded points:

$$\begin{aligned} f_{occ} &= MLP_{shs}(h_{agg}, \gamma(x_{occ})) \\ \alpha_{occ} &= MLP_{opacity}(h_{agg}, \gamma(x_{occ})), \end{aligned} \quad (11)$$

Where $\gamma()$ represents the positional encoding [47], we will replace the spherical harmonic coefficient and opacity of occluded point with the output of MLP_{shs} and $MLP_{opacity}$.

3.5 Training Strategy

Loss Function. Following other methods using 3DGS to render human, we introduce RGB loss \mathcal{L}_{color} , mask loss \mathcal{L}_{mask} , SSIM loss \mathcal{L}_{SSIM} [50], and LPIPS loss \mathcal{L}_{LPIPS} [68] to supervise the network on the visible human parts which having ground truth, we define these losses as $\mathcal{L}_{standard}$:

$$\mathcal{L}_{standard} = \mathcal{L}_{rgb} + \lambda_1 \mathcal{L}_{mask} + \lambda_2 \mathcal{L}_{SSIM} + \lambda_3 \mathcal{L}_{LPIPS}, \quad (12)$$

However, for occluded regions where ground truth does not exist, these losses will become ineffective. Hence, it is necessary to design loss specifically for occluded areas. Inspired by the occlusion decoupling loss purposed in wild2avatar [54], we design the occlusion loss \mathcal{L}_{occ} . The process of \mathcal{L}_{occ} is shown in Figure 4. The approach involves projecting the points onto the image plane to obtain a body mask α_{body} that roughly describes the outline of the human body. For

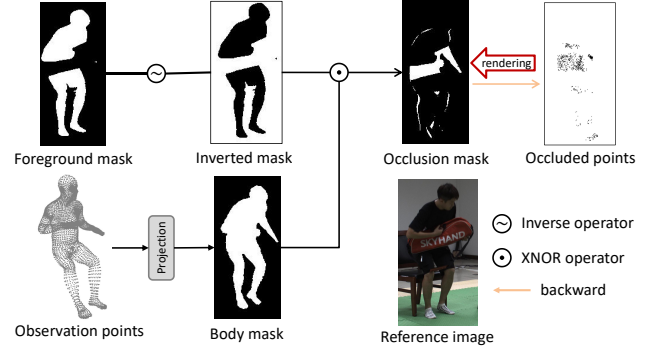


Figure 4. The process of \mathcal{L}_{occ} . The observation points are projected to get a rough human body mask α_{body} . By performing a logical OR operation between this mask and the inverse of the foreground mask α_{fg} , we obtain an approximate mask α_{occ} describing occluded objects. Then we render the occluded points and calculate the loss between the two. the occluded foreground mask α_{fg} , we compute its inversion and perform an XOR operation between α_{body} and the inversion of α_{fg} , resulting in an occlusion mask α_{occ} that roughly describes the occluded region. As we project points onto the image plane, we can extract points that lie in the occluded region, render them and calculate loss between the rendered alpha mask α_{render_occ} and the occlusion mask α_{occ} . In summary, our α_{occ} and \mathcal{L}_{occ} are defined as:

$$\begin{aligned} \alpha_{occ} &= \alpha_{body} \odot (\sim \alpha_{fg}) \\ \mathcal{L}_{occ} &= MSE(\alpha_{render_occ}, \alpha_{occ}), \end{aligned} \quad (13)$$

Where \odot is the XOR operation. In addition, we observing that after the adaptive density control, some points with small opacity in occluded regions are pruned, which should be retained. For these points under the opacity threshold ϵ , we render them to obtain $\hat{C}_{s_opacity}$ and $\hat{\alpha}_{s_opacity}$, and calculate the consistency loss \mathcal{L}_{con} with RGB ground truth C and mask ground truth α :

$$\mathcal{L}_{con} = |\hat{C}_{s_opacity} - C| + \lambda_{con} MSE(\hat{\alpha}_{s_opacity}, \alpha), \quad (14)$$

where we set the opacity threshold as $\epsilon = 0.05$ and $\lambda_{con} = 0.1$. Our total loss function \mathcal{L}_{total} is defined as:

$$\mathcal{L}_{total} = \mathcal{L}_{standard} + \lambda_4 \mathcal{L}_{occ} + \mathcal{L}_{con}, \quad (15)$$

Here we set $\lambda_1 = \lambda_2 = \lambda_3 = \lambda_4 = 0.1$. For more details about the loss functions, please refer to the appendix.

3D Gaussian Optimization. 3DGS uses SfM [43] sparse point clouds to initialize Gaussian distributions. In the human rendering task, it is more reasonable to initialize Gaussian distributions using $N = 6890$ SMPL vertices in the canonical space, which contains more prior information about human [15, 40]. Additionally, we follow the adaptive density control in gauhuman [15] which involves: (1) constraining split and clone based on KL divergence, (2) introducing merge operation to merge redundant points, and (3) prune the points which are far from the SMPL surface. Please refer to the appendix for details.



Figure 5. Qualitative results between our OccGaussian and OccNeRF on ZJU-MoCap and OcMotion datasets.

Table 1. Quantitative comparison of ours and baseline methods on the ZJU-MoCap and OcMotion datasets. SOTA metric are bold. LPIPS* = $1000 \times$ LPIPS.

Method	ZJU_MoCap					OcMotion				
	PSNR \uparrow	SSIM \uparrow	LPIPS* \downarrow	Train	FPS	PSNR \uparrow	SSIM \uparrow	LPIPS* \downarrow	Train	FPS
HumanNeRF [51]	20.67	0.9509	-	-	-	19.57	0.9575	-	-	-
OccNeRF [55]	22.40	0.9562	43.01	28h~40h	0.20	21.01	0.9668	38.14	25h	0.16
OccGaussian(Ours)	23.29	0.9482	41.93	6m	169	21.76	0.9657	32.18	13m	163

4 Experiments

4.1 Implementation Details

We adopt the pre-trained ResNet18 [12] as the 2D image encoder. We train for 2400 iterations on the ZJU-MoCap dataset [38]. And for the OcMotion dataset [16], due to the more complex and various occlusions, we train for 5000 iterations. Utilizing the loss functions proposed in Section

3.5, we optimize OccGaussian using the Adam optimizer [20] and dynamically adjust the learning rate based on the training steps. Please refer to the appendix for more details.

4.2 Datasets

ZJU-MoCap [38]. The ZJU-Mocap dataset is a widely used benchmark in human modeling, supplying human masks and SMPL parameters. We select six human subjects (377,

386, 387, 392, 393, 394) to conduct experiments and adopt the same training and testing setting as OccNeRF [55], i.e., the first camera is used for training, and the remaining cameras are used for evaluation. Since ZJU-MoCap is captured in a lab environment, there is no occlusion, so we simulate occlusions on training data following OccNeRF. This is done by artificially placing a rectangular barrier between the camera and the human, which is centered at the mean center of all valid pixels from the video frame and will obscure 50% of the valid pixels. The length of the rectangle is the length of the image, and the center and width vary for different subjects. We set the obstacle to stationary and added this occlusion on 80% of training frames. More details is provided in appendix. **OcMotion** [16]. The OcMotion dataset is built for human pose estimation under occlusion, which contains 43 motions and 300K frames with 3D annotations. This dataset better presents what happens when people encounter occlusion in real-life scenarios. Following OccNeRF, we evaluating on two videos with different levels of occlusions. 500 frames from video 11, camera 2 is defined as **mild** occlusion video, and 540 frames from video 14, camera 4 is defined as **severe** occlusion video. We use the camera parameters and SMPL parameters provided by OcMotion.

4.3 Comparison and Metrics

The state-of-art occluded human rendering method is OccNeRF [55], which we mainly compare with. And we also test the rendering performance of 3DGS-Avatar [40] directly on occluded human. All the methods use the same training and evaluation setting, including a single training view, using foreground human mask and SMPL/camera parameters in training. Methods are compared qualitatively and quantitatively, for qualitative evaluations, we synthesize novel views to compare the quality of renderings. For quantitative evaluations, we consider three commonly used metrics: peak signal-to-noise ratio (PSNR), structural similarity (SSIM) [50] and LPIPS [68] to measure the rendering quality. To demonstrate the superiority of our approach, we also calculating the training time and the Frames Per Second (FPS) of rendering. Note that the OcMotion dataset doesn't have non-occlusive ground truth, we only calculate metrics on the visible area.

4.4 Qualitative Results

In Figure 5, we present the novel view rendering results of our OccGaussian and OccNeRF. For the ZJU-MoCap dataset with simulated occlusions, both our OccGaussian and OccNeRF are capable of rendering a mostly complete body geometry. However, OccNeRF sometimes fails to fill reasonable details in occluded regions, resulting in poor continuity of generated textures and will render some artifacts or floats on the body surface. By enhancing the input 2D observation information, OccGaussian complements texture in occluded regions, better recovering the facial expressions and clothing details with less artifacts. For the OcMotion

dataset with real-world occlusions, although the quality of rendering somehow declined, OccGaussian is still able to render a relatively complete body with occluded area recovered. However OccNeRF will miss certain body parts (such as hands) and produce much more artifacts and noise. It also shows that our method still performs well in the real-world scenarios. Please refer to the appendix for more qualitative results.

4.5 Quantitative Results

We summarize the overall novel view synthesis results of our OccGaussian, OccNeRF and HumanNeRF in Table 1; the metrics are mean values taken on all subjects. Benefiting from 3DGS, our OccGaussian can train within minutes, while OccNeRF requires over one day to train, we accelerate by nearly 250 times. And OccNeRF takes 5 to 6 seconds to render an image when synthesizing novel views, limiting its real-world applications. In contrast, our method achieves a maximum FPS of 169, capable of rendering hundreds of frames in seconds which is 800 times faster than OccNeRF. For the evaluation metrics, Our approach achieves SOTA in both PSNR and LPIPS compare to OccNeRF, demonstrating that OccGaussian remains competitive in rendering quality while significantly reducing the time for training and rendering. We don't provide some specific metrics for HumanNeRF, because the LPIPS is not measured in OccNeRF, and both training time and FPS are roughly equivalent to OccNeRF. Table 2 provides a more detailed summary for OccGaussian and OccNeRF, we can see our approach outperforms OccNeRF in PSNR and LPIPS across all subjects.

4.6 Ablation Studies

We are conducting ablation experiments by removing the methods proposed in Chapter 3 to demonstrate their effectiveness in improving rendering quality. We present qualitative results of video **severe** from OcMotion in Figure 6. And since the OcMotion dataset doesn't capture complete images that are not occluded, we provide quantitative results on the ZJU-MoCap dataset in Table 3, it's mean values taken on all subjects.

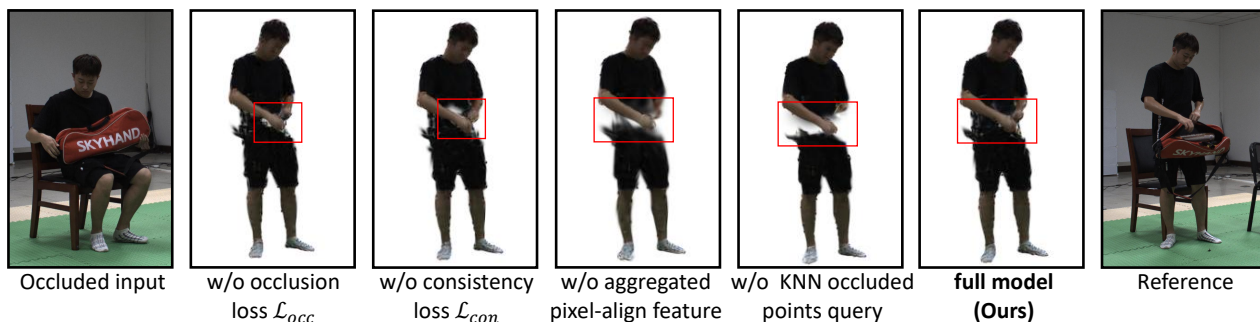
Occlusion Loss \mathcal{L}_{occ} and consistency loss \mathcal{L}_{con} . Our proposed \mathcal{L}_{occ} and \mathcal{L}_{con} contribute to improving rendering quality in occluded area. After removing these two losses, the density of rendering decreases faintly near the occluded regions, and there is a slight decline in metrics.

Aggregated Pixel-Aligned Feature. The aggregated pixel-align feature can more fully utilize the feature of visible points to recover the occluded region. After deactivating it, we replace the spherical harmonic coefficient and opacity of the occluded point with those of the KNN visible points, weighted by their respective distances. We can see there is a large amount missing in the occluded region after the feature is disabled, the model will only partially render some unrealistic artifacts in these areas.

Table 2. Quantitative comparison between ours and OccNeRF on ZJU-MoCap and OcMotion datasets.

ZJU-MoCap	Subject 377			Subject 386			Subject 387		
	PSNR	SSIM	LPIPS*	PSNR	SSIM	LPIPS*	PSNR	SSIM	LPIPS*
OccNeRF [55]	23.37	0.9648	34.23	23.43	0.9629	41.87	22.15	0.9506	44.58
OccGaussian	24.33	0.9589	32.43	24.11	0.9544	39.36	23.02	0.9422	44.47
ZJU-MoCap	Subject 392			Subject 393			Subject 394		
	PSNR	SSIM	LPIPS*	PSNR	SSIM	LPIPS*	PSNR	SSIM	LPIPS*
OccNeRF [55]	22.13	0.9578	44.56	21.40	0.9484	47.82	21.95	0.9527	45.02
OccGaussian	22.92	0.9481	44.07	22.50	0.9413	46.87	22.84	0.9444	44.38

OcMotion	Video Mild			Video Severe		
	PSNR	SSIM	LPIPS*	PSNR	SSIM	LPIPS*
OccNeRF [55]	21.55	0.9700	36.07	20.48	0.9637	40.21
OccGaussian	22.59	0.9702	30.04	20.93	0.9612	34.32

**Figure 6.** Qualitative results of ablation study on the Video Severe of OcMotion dataset.

KNN Occluded Points Query. With the KNN occluded points query disabled, it is equivalent to rendering the occluded region directly without any processing. This time, the occluded region will be treated as background during training, and the appearance of the occluded region will not be rendered at all. Also, the metrics are the worst among all.

Table 3. Quantitative results of ablation study on the ZJU-MoCap dataset.

	PSNR↑	SSIM↑	LPIPS*↓
Full model(Ours)	23.29	0.9482	41.93
w/o \mathcal{L}_{occ} and \mathcal{L}_{con}	23.03	0.9471	42.84
w/o aggregated pixel-align feature	22.58	0.9460	46.04
w/o KNN occluded points query	18.42	0.9367	53.84

5 Discussions

Rendering high-quality humans under monocular occluded videos is exceptionally challenging. Facing with occlusions of varying shapes, and the occluded region has neither ground truth nor information to supplement from other views. By querying the features of neighboring visible points, our OccGaussian is able to render a complete human body geometry. However, if the regions have occluded for extended periods,

OccGaussian still can't fully recover them, resulting in some defects because the supervision in these regions is too weak. This issue may be addressed by incorporating temporal information [53]. Additionally, our method requires relatively accurate human poses and camera parameters to project 3D points, in-the-wild videos with inaccurate priors can also degrade the rendering quality.

6 Conclusion

We propose OccGaussian, the first method to render human in monocular videos with occlusions using 3D Gaussian Splatting. While previous methods are too time-consuming in training and inference to meet the requirements of real-time applications, we can achieve fast training (6 ~ 13 minutes) and real-time rendering (169 FPS). Specifically, we perform feature query in the occluded region, and input the aggregated pixel-align feature of visible K-nearest points into MLP to learn the information of invisible points. Moreover, we design the specialized loss functions for the occluded region, which makes the rendering more complete. In our experiments, we compare OccGaussian with the SOTA method under both simulated and real-world occlusions. The experiments show that our OccGaussian achieves SOTA performance while maintaining fast training and real-time rendering.

References

- [1] Kara-Ali Aliev, Artem Sevastopolsky, Maria Kolos, Dmitry Ulyanov, and Victor Lempitsky. 2020. Neural point-based graphics. In *Computer Vision—ECCV 2020: 16th European Conference, Glasgow, UK, August 23–28, 2020, Proceedings, Part XXII* 16. Springer, 696–712.
- [2] Jonathan T Barron, Ben Mildenhall, Matthew Tancik, Peter Hedman, Ricardo Martin-Brualla, and Pratul P Srinivasan. 2021. Mip-nerf: A multiscale representation for anti-aliasing neural radiance fields. In *Proceedings of the IEEE/CVF International Conference on Computer Vision*. 5855–5864.
- [3] Jonathan T Barron, Ben Mildenhall, Dor Verbin, Pratul P Srinivasan, and Peter Hedman. 2022. Mip-nerf 360: Unbounded anti-aliased neural radiance fields. In *Proceedings of the IEEE/CVF Conference on Computer Vision and Pattern Recognition*. 5470–5479.
- [4] Jianchuan Chen, Wentao Yi, Liqian Ma, Xu Jia, and Huchuan Lu. 2023. GM-NeRF: Learning Generalizable Model-based Neural Radiance Fields from Multi-view Images. In *Proceedings of the IEEE/CVF Conference on Computer Vision and Pattern Recognition*. 20648–20658.
- [5] Mingfei Chen, Jianfeng Zhang, Xiangyu Xu, Lijuan Liu, Yujun Cai, Jiashi Feng, and Shuicheng Yan. 2022. Geometry-guided progressive nerf for generalizable and efficient neural human rendering. In *European Conference on Computer Vision*. Springer, 222–239.
- [6] Xu Chen, Yufeng Zheng, Michael J Black, Otmar Hilliges, and Andreas Geiger. 2021. Snarf: Differentiable forward skinning for animating non-rigid neural implicit shapes. In *Proceedings of the IEEE/CVF International Conference on Computer Vision*. 11594–11604.
- [7] Yue Chen, Xuan Wang, Xingyu Chen, Qi Zhang, Xiaoyu Li, Yu Guo, Jue Wang, and Fei Wang. 2023. UV Volumes for real-time rendering of editable free-view human performance. In *Proceedings of the IEEE/CVF Conference on Computer Vision and Pattern Recognition*. 16621–16631.
- [8] Sara Fridovich-Keil, Alex Yu, Matthew Tancik, Qinzhong Chen, Benjamin Recht, and Angjoo Kanazawa. 2022. Plenoxels: Radiance fields without neural networks. In *Proceedings of the IEEE/CVF Conference on Computer Vision and Pattern Recognition*. 5501–5510.
- [9] Chen Geng, Sida Peng, Zhen Xu, Hujun Bao, and Xiaowei Zhou. 2023. Learning neural volumetric representations of dynamic humans in minutes. In *Proceedings of the IEEE/CVF Conference on Computer Vision and Pattern Recognition*. 8759–8770.
- [10] Markus Gross and Hanspeter Pfister. 2011. *Point-based graphics*. Elsevier.
- [11] Rıza Alp Güler, Natalia Neverova, and Iasonas Kokkinos. 2018. Densepose: Dense human pose estimation in the wild. In *Proceedings of the IEEE conference on computer vision and pattern recognition*. 7297–7306.
- [12] Kaiming He, Xiangyu Zhang, Shaoqing Ren, and Jian Sun. 2016. Deep residual learning for image recognition. In *Proceedings of the IEEE conference on computer vision and pattern recognition*. 770–778.
- [13] Liangxiao Hu, Hongwen Zhang, Yuxiang Zhang, Boyao Zhou, Boning Liu, Shengping Zhang, and Liqiang Nie. 2023. Gaussianavatar: Towards realistic human avatar modeling from a single video via animatable 3d gaussians. *arXiv preprint arXiv:2312.02134* (2023).
- [14] Shoukang Hu, Fangzhou Hong, Liang Pan, Haiyi Mei, Lei Yang, and Ziwei Liu. 2023. SHERF: Generalizable Human NeRF from a Single Image. *arXiv preprint arXiv:2303.12791* (2023).
- [15] Shoukang Hu and Ziwei Liu. 2023. Gauhuman: Articulated gaussian splatting from monocular human videos. *arXiv preprint arXiv:2312.02973* (2023).
- [16] Buzhen Huang, Yuan Shu, Jingyi Ju, and Yangang Wang. 2022. Occluded Human Body Capture with Self-Supervised Spatial-Temporal Motion Prior. *arXiv preprint arXiv:2207.05375* (2022).
- [17] Tianjian Jiang, Xu Chen, Jie Song, and Otmar Hilliges. 2023. Instantavatar: Learning avatars from monocular video in 60 seconds. In *Proceedings of the IEEE/CVF Conference on Computer Vision and Pattern Recognition*. 16922–16932.
- [18] Yuheng Jiang, Zehao Shen, Penghao Wang, Zhuo Su, Yu Hong, Yingliang Zhang, Jingyi Yu, and Lan Xu. 2023. Hifi4g: High-fidelity human performance rendering via compact gaussian splatting. *arXiv preprint arXiv:2312.03461* (2023).
- [19] Bernhard Kerbl, Georgios Kopanas, Thomas Leimkühler, and George Drettakis. 2023. 3D Gaussian Splatting for Real-Time Radiance Field Rendering. *ACM Transactions on Graphics* 42, 4 (2023).
- [20] Diederik P Kingma and Jimmy Ba. 2014. Adam: A method for stochastic optimization. *arXiv preprint arXiv:1412.6980* (2014).
- [21] Muhammed Kocabas, Jen-Hao Rick Chang, James Gabriel, Oncel Tuzel, and Anurag Ranjan. 2023. Hugs: Human gaussian splats. *arXiv preprint arXiv:2311.17910* (2023).
- [22] Youngjoong Kwon, Dahun Kim, Duygu Ceylan, and Henry Fuchs. 2021. Neural human performer: Learning generalizable radiance fields for human performance rendering. *Advances in Neural Information Processing Systems* 34 (2021), 24741–24752.
- [23] Jiahui Lei, Yufu Wang, Georgios Pavlakos, Lingjie Liu, and Kostas Daniilidis. 2023. Gart: Gaussian articulated template models. *arXiv preprint arXiv:2311.16099* (2023).
- [24] Mingwei Li, Jiachen Tao, Zongxin Yang, and Yi Yang. 2023. Human101: Training 100+ fps human gaussians in 100s from 1 view. *arXiv preprint arXiv:2312.15258* (2023).
- [25] Tianye Li, Timo Bolkart, Michael J Black, Hao Li, and Javier Romero. 2017. Learning a model of facial shape and expression from 4D scans. *ACM Trans. Graph.* 36, 6 (2017), 194–1.
- [26] Zhe Li, Zerong Zheng, Lizhen Wang, and Yebin Liu. 2023. Animatable gaussians: Learning pose-dependent gaussian maps for high-fidelity human avatar modeling. *arXiv preprint arXiv:2311.16096* (2023).
- [27] Hanbing Liu, Jun-Yan He, Zhi-Qi Cheng, Wangmeng Xiang, Qize Yang, Wenhao Chai, Gaoang Wang, Xu Bao, Bin Luo, Yifeng Geng, et al. 2023. Posynda: Multi-hypothesis pose synthesis domain adaptation for robust 3d human pose estimation. In *Proceedings of the 31st ACM International Conference on Multimedia*. 5542–5551.
- [28] Matthew Loper, Naureen Mahmood, Javier Romero, Gerard Pons-Moll, and Michael J Black. 2023. SMPL: A skinned multi-person linear model. In *Seminal Graphics Papers: Pushing the Boundaries, Volume 2*. 851–866.
- [29] Jonathon Luiten, Georgios Kopanas, Bastian Leibe, and Deva Ramanan. 2023. Dynamic 3d gaussians: Tracking by persistent dynamic view synthesis. *arXiv preprint arXiv:2308.09713* (2023).
- [30] Marko Mihajlovic, Aayush Bansal, Michael Zollhoefer, Siyu Tang, and Shunsuke Saito. 2022. KeypointNeRF: Generalizing image-based volumetric avatars using relative spatial encoding of keypoints. In *European conference on computer vision*. Springer, 179–197.
- [31] Ben Mildenhall, Pratul P Srinivasan, Matthew Tancik, Jonathan T Barron, Ravi Ramamoorthi, and Ren Ng. 2021. Nerf: Representing scenes as neural radiance fields for view synthesis. *Commun. ACM* 65, 1 (2021), 99–106.
- [32] Arthur Moreau, Jifei Song, Helisa Dharmo, Richard Shaw, Yiren Zhou, and Eduardo Pérez-Pellitero. 2023. Human gaussian splatting: Real-time rendering of animatable avatars. *arXiv preprint arXiv:2311.17113* (2023).
- [33] Thomas Müller, Alex Evans, Christoph Schied, and Alexander Keller. 2022. Instant neural graphics primitives with a multiresolution hash encoding. *ACM Transactions on Graphics (ToG)* 41, 4 (2022), 1–15.
- [34] Xiao Pan, Zongxin Yang, Jianxin Ma, Chang Zhou, and Yi Yang. 2023. Transhuman: A transformer-based human representation for generalizable neural human rendering. In *Proceedings of the IEEE/CVF International conference on computer vision*. 3544–3555.
- [35] Haokai Pang, Heming Zhu, Adam Kortylewski, Christian Theobalt, and Marc Habermann. 2023. Ash: Animatable gaussian splats for efficient and photoreal human rendering. *arXiv preprint arXiv:2312.05941* (2023).
- [36] Georgios Pavlakos, Vasileios Choutas, Nima Ghorbani, Timo Bolkart, Ahmed AA Osman, Dimitrios Tzionas, and Michael J Black. 2019.

- Expressive body capture: 3d hands, face, and body from a single image. In *Proceedings of the IEEE/CVF conference on computer vision and pattern recognition*. 10975–10985.
- [37] Sida Peng, Junting Dong, Qianqian Wang, Shangzhan Zhang, Qing Shuai, Xiaowei Zhou, and Hujun Bao. 2021. Animatable neural radiance fields for modeling dynamic human bodies. In *Proceedings of the IEEE/CVF International Conference on Computer Vision*. 14314–14323.
- [38] Sida Peng, Yuanqing Zhang, Yinghao Xu, Qianqian Wang, Qing Shuai, Hujun Bao, and Xiaowei Zhou. 2021. Neural body: Implicit neural representations with structured latent codes for novel view synthesis of dynamic humans. In *Proceedings of the IEEE/CVF Conference on Computer Vision and Pattern Recognition*. 9054–9063.
- [39] Shenhan Qian, Tobias Kirschstein, Liam Schoneveld, Davide Davoli, Simon Giebenhain, and Matthias Nießner. 2023. Gaussianavatars: Photorealistic head avatars with rigged 3d gaussians. *arXiv preprint arXiv:2312.02069* (2023).
- [40] Zhiyin Qian, Shaofei Wang, Marko Mihajlovic, Andreas Geiger, and Siyu Tang. 2023. 3dgs-avatar: Animatable avatars via deformable 3d gaussian splatting. *arXiv preprint arXiv:2312.09228* (2023).
- [41] Javier Romero, Dimitrios Tzionas, and Michael J Black. 2022. Embodied hands: Modeling and capturing hands and bodies together. *arXiv preprint arXiv:2201.02610* (2022).
- [42] Darius Rückert, Linus Franke, and Marc Stamminger. 2022. Adop: Approximate differentiable one-pixel point rendering. *ACM Transactions on Graphics (ToG)* 41, 4 (2022), 1–14.
- [43] Johannes L Schonberger and Jan-Michael Frahm. 2016. Structure-from-motion revisited. In *Proceedings of the IEEE conference on computer vision and pattern recognition*. 4104–4113.
- [44] Gyumin Shim, Minsoo Lee, and Jaegul Choo. 2022. Refu: Refine and fuse the unobserved view for detail-preserving single-image 3d human reconstruction. In *Proceedings of the 30th ACM International Conference on Multimedia*. 6850–6859.
- [45] Shih-Yang Su, Timur Bagautdinov, and Helge Rhodin. 2023. NPC: Neural Point Characters from Video. *arXiv preprint arXiv:2304.02013* (2023).
- [46] Guoxing Sun, Xin Chen, Yizhang Chen, Anqi Pang, Pei Lin, Yuheng Jiang, Lan Xu, Jingyi Yu, and Jingya Wang. 2021. Neural free-viewpoint performance rendering under complex human-object interactions. In *Proceedings of the 29th ACM International Conference on Multimedia*. 4651–4660.
- [47] Ashish Vaswani, Noam Shazeer, Niki Parmar, Jakob Uszkoreit, Llion Jones, Aidan N Gomez, Łukasz Kaiser, and Illia Polosukhin. 2017. Attention is all you need. *Advances in neural information processing systems* 30 (2017).
- [48] Haonan Wang, Jie Liu, Jie Tang, and Gangshan Wu. 2023. Lightweight Super-Resolution Head for Human Pose Estimation. In *Proceedings of the 31st ACM International Conference on Multimedia*. 2353–2361.
- [49] Liao Wang, Ziyu Wang, Pei Lin, Yuheng Jiang, Xin Suo, Minye Wu, Lan Xu, and Jingyi Yu. 2021. ibutter: Neural interactive bullet time generator for human free-viewpoint rendering. In *Proceedings of the 29th ACM International Conference on Multimedia*. 4641–4650.
- [50] Zhou Wang, Alan C Bovik, Hamid R Sheikh, and Eero P Simoncelli. 2004. Image quality assessment: from error visibility to structural similarity. *IEEE transactions on image processing* 13, 4 (2004), 600–612.
- [51] Chung-Yi Weng, Brian Curless, Pratul P Srinivasan, Jonathan T Barron, and Ira Kemelmacher-Shlizerman. 2022. Humannerf: Free-viewpoint rendering of moving people from monocular video. In *Proceedings of the IEEE/CVF conference on computer vision and pattern recognition*. 16210–16220.
- [52] Chung-Yi Weng, Pratul P Srinivasan, Brian Curless, and Ira Kemelmacher-Shlizerman. 2023. PersonNeRF: Personalized Reconstruction from Photo Collections. In *Proceedings of the IEEE/CVF Conference on Computer Vision and Pattern Recognition*. 524–533.
- [53] Guanjun Wu, Taoran Yi, Jiemin Fang, Lingxi Xie, Xiaopeng Zhang, Wei Wei, Wenyu Liu, Qi Tian, and Xinggang Wang. 2023. 4d gaussian splatting for real-time dynamic scene rendering. *arXiv preprint arXiv:2310.08528* (2023).
- [54] Tiange Xiang, Adam Sun, Scott Delp, Kazuki Kozuka, Li Fei-Fei, and Ehsan Adeli. 2023. Wild2Avatar: Rendering Humans Behind Occlusions. *arXiv preprint arXiv:2401.00431* (2023).
- [55] Tiange Xiang, Adam Sun, Jiajun Wu, Ehsan Adeli, and Li Fei-Fei. 2023. Rendering humans from object-occluded monocular videos. In *Proceedings of the IEEE/CVF International Conference on Computer Vision*. 3239–3250.
- [56] Hongyi Xu, Eduard Gabriel Bazavan, Andrei Zanfir, William T Freeman, Rahul Sukthankar, and Cristian Sminchisescu. 2020. Ghum & ghuml: Generative 3d human shape and articulated pose models. In *Proceedings of the IEEE/CVF Conference on Computer Vision and Pattern Recognition*. 6184–6193.
- [57] Qianguang Xu, Zexiang Xu, Julien Philip, Sai Bi, Zhixun Shu, Kalyan Sunkavalli, and Ulrich Neumann. 2022. Point-nerf: Point-based neural radiance fields. In *Proceedings of the IEEE/CVF Conference on Computer Vision and Pattern Recognition*. 5438–5448.
- [58] Yuelang Xu, Benwang Chen, Zhe Li, Hongwen Zhang, Lizhen Wang, Zerong Zheng, and Yebin Liu. 2023. Gaussian head avatar: Ultra high-fidelity head avatar via dynamic gaussians. *arXiv preprint arXiv:2312.03029* (2023).
- [59] Yuelang Xu, Hongwen Zhang, Lizhen Wang, Xiaochen Zhao, Han Huang, Guojun Qi, and Yebin Liu. 2023. LatentAvatar: Learning Latent Expression Code for Expressive Neural Head Avatar. *arXiv preprint arXiv:2305.01190* (2023).
- [60] Kaibing Yang, Renshu Gu, Maoyu Wang, Masahiro Toyoura, and Gang Xu. 2022. LASOR: Learning accurate 3D human pose and shape via synthetic occlusion-aware data and neural mesh rendering. *IEEE Transactions on Image Processing* 31 (2022), 1938–1948.
- [61] Ziyi Yang, Xinyu Gao, Wen Zhou, Shaohui Jiao, Yuqing Zhang, and Xiaogang Jin. 2023. Deformable 3d gaussians for high-fidelity monocular dynamic scene reconstruction. *arXiv preprint arXiv:2309.13101* (2023).
- [62] Ze Yang, Shenlong Wang, Sivabalan Manivasagam, Zeng Huang, Wei-Chiu Ma, Xinchun Yan, Ersin Yumer, and Raquel Urtasun. 2021. S3: Neural shape, skeleton, and skinning fields for 3d human modeling. In *Proceedings of the IEEE/CVF conference on computer vision and pattern recognition*. 13284–13293.
- [63] Wang Yifan, Felice Serena, Shihao Wu, Cengiz Öztireli, and Olga Sorkine-Hornung. 2019. Differentiable surface splatting for point-based geometry processing. *ACM Transactions on Graphics (TOG)* 38, 6 (2019), 1–14.
- [64] Zhengming Yu, Wei Cheng, Xian Liu, Wayne Wu, and Kwan-Yee Lin. 2023. MonoHuman: Animatable Human Neural Field from Monocular Video. In *Proceedings of the IEEE/CVF Conference on Computer Vision and Pattern Recognition*. 16943–16953.
- [65] Ye Yuan, Xueting Li, Yangyi Huang, Shalini De Mello, Koki Nagano, Jan Kautz, and Umar Iqbal. 2023. Gavatar: Animatable 3d gaussian avatars with implicit mesh learning. *arXiv preprint arXiv:2312.11461* (2023).
- [66] Juze Zhang, Jingya Wang, Ye Shi, Fei Gao, Lan Xu, and Jingyi Yu. 2022. Mutual Adaptive Reasoning for Monocular 3D Multi-Person Pose Estimation. In *Proceedings of the 30th ACM International Conference on Multimedia*. 1788–1796.
- [67] Jiahui Zhang, Fangneng Zhan, Rongliang Wu, Yingchen Yu, Wenqing Zhang, Bai Song, Xiaoqin Zhang, and Shijian Lu. 2022. Vmrf: View matching neural radiance fields. In *Proceedings of the 30th ACM International Conference on Multimedia*. 6579–6587.
- [68] Richard Zhang, Phillip Isola, Alexei A Efros, Eli Shechtman, and Oliver Wang. 2018. The unreasonable effectiveness of deep features as a perceptual metric. In *Proceedings of the IEEE conference on computer*

- vision and pattern recognition*. 586–595.
- [69] Fuqiang Zhao, Wei Yang, Jiakai Zhang, Pei Lin, Yingliang Zhang, Jingyi Yu, and Lan Xu. 2022. Humannerf: Efficiently generated human radiance field from sparse inputs. In *Proceedings of the IEEE/CVF Conference on Computer Vision and Pattern Recognition*. 7743–7753.
- [70] Shunyuan Zheng, Boyao Zhou, Ruizhi Shao, Boning Liu, Shengping Zhang, Liqiang Nie, and Yebin Liu. 2023. Gps-gaussian: Generalizable pixel-wise 3d gaussian splatting for real-time human novel view synthesis. *arXiv preprint arXiv:2312.02155* (2023).
- [71] Yufeng Zheng, Victoria Fernández Abrevaya, Marcel C Bühler, Xu Chen, Michael J Black, and Otmar Hilliges. 2022. Im avatar: Implicit morphable head avatars from videos. In *Proceedings of the IEEE/CVF Conference on Computer Vision and Pattern Recognition*. 13545–13555.
- [72] Yufeng Zheng, Wang Yifan, Gordon Wetzstein, Michael J Black, and Otmar Hilliges. 2023. Pointavatar: Deformable point-based head avatars from videos. In *Proceedings of the IEEE/CVF Conference on Computer Vision and Pattern Recognition*. 21057–21067.
- [73] Qiang Zhou, Shiyin Wang, Yitong Wang, Zilong Huang, and Xinggang Wang. 2021. Human de-occlusion: Invisible perception and recovery for humans. In *Proceedings of the IEEE/CVF Conference on Computer Vision and Pattern Recognition*. 3691–3701.

A Supplementary Material

A.1 Definition of Occlusions

This definition of occlusions is followed by OccNeRF [55]. For simulated occlusions (ZJU-MoCap), we define the extent of occlusion as $1 - \frac{\text{occluded pixels}}{\text{valid pixels}}$. For real-world occlusions (OcMotion), where there is no reference for the occluded body, we utilize 2D projections of the ground truth SMPL mesh. In this case, the occlusion extent is defined as $1 - \frac{\text{visible pixels} \cap \text{SMPL pixels}}{\text{SMPL pixels}}$. Using the above formula, The occlusion extents for video **Mild** and video **Severe** are 17% and 79%, respectively.

A.2 The Structures of $MLP_{opacity}$ and MLP_{shs}

We used MLP_{shs} and $MLP_{opacity}$ to learn the spherical harmonic coefficients f and opacity α of the invisible points, respectively. The structures of $MLP_{opacity}$ and MLP_{shs} are identical, we outlined the architecture in Figure 7. It’s a five-layer MLP with an input layer, an output layer, and three hidden layers. The dimensions of the hidden layers are 256, and residual connections are employed within the three hidden layers. The output dimensions of $MLP_{opacity}$ and MLP_{shs} are $\alpha \in \mathcal{R}^1$ and $f \in \mathcal{R}^{3 \times 16}$ respectively, and the learning rate of MLP is set to 5×10^{-4} .

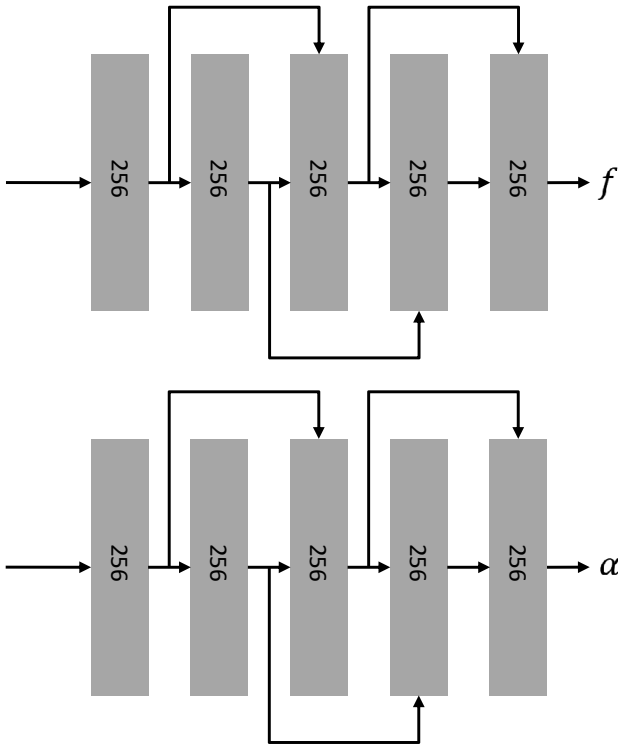


Figure 7. The network structure of $MLP_{opacity}$ and MLP_{shs} .

A.3 3D Gaussian Optimization

The superior rendering quality of 3DGS [19] relies heavily on the adaptive density control of 3D Gaussians. Following Gauhuman [15], we select points with large KL divergence and positional gradients to perform the split and clone. The KL divergence of two Gaussians is calculated as:

$$KL(G(x_0)|G(x_1)) = \frac{1}{2}(\text{tr}(\Sigma_1^{-1}\Sigma_0) + \ln \frac{\det \Sigma_1}{\det \Sigma_2} + (\mu_1 - \mu_0)^T \Sigma_1^{-1}(\mu_1 - \mu_0) - 3), \quad (16)$$

where $\mu_0, \Sigma_0, \mu_1, \Sigma_1$ are the mean and covariance matrix of two 3D Gaussians $G(x_0)$ and $G(x_1)$. We further follow the merge operation from Gauhuman, 3D Gaussians with 1) large position gradients, 2) small scaling magnitude, and 3) KL divergence less than 0.1 will be merged. Two Gaussians are merged by averaging their means, opacity, and SH coefficients.

A.4 Details of Loss Functions

Photometric Loss. Given the ground truth target image C and predicted image \hat{C} , we apply the photometric loss:

$$\mathcal{L}_{rgb} = |\hat{C} - C|. \quad (17)$$

Mask Loss. We also leverage the human region masks for Human NeRF optimization. The mask loss is defined as:

$$\mathcal{L}_{mask} = \|\hat{M} - M\|_2, \quad (18)$$

where \hat{M} is the accumulated volume density and M is the ground truth binary mask label.

SSIM Loss. We further employ SSIM [50] to ensure the structural similarity between ground truth and synthesized images:

$$\mathcal{L}_{SSIM} = \text{SSIM}(\hat{C}, C). \quad (19)$$

LPIPS Loss. The perceptual loss LPIPS [68] is also utilized to ensure the quality of the rendered image:

$$\mathcal{L}_{LPIPS} = \text{LPIPS}(\hat{C}, C). \quad (20)$$

Details about α_{body} . In order to obtain an approximate description of the complete body, we project 3D points onto the 2D image plane and set the radius of each point to two pixels to ensure that adjacent points can be connected to each other. Now we have obtained a complete body mask, but due to the large radius of each point, the mask appears too bulky. Therefore, we further perform an erosion operation on the mask to obtain our α_{body} , with an erosion kernel size chosen as 5×5 . The masks before and after erosion are shown in Figure 9.

A.5 Ablation Results for K-nearest Occluded Points Query

When conducting the Occlusion Feature Query in section 3.3, we need to find the nearest k visible points for each occluded point. To this end, we conducted ablation experiments to

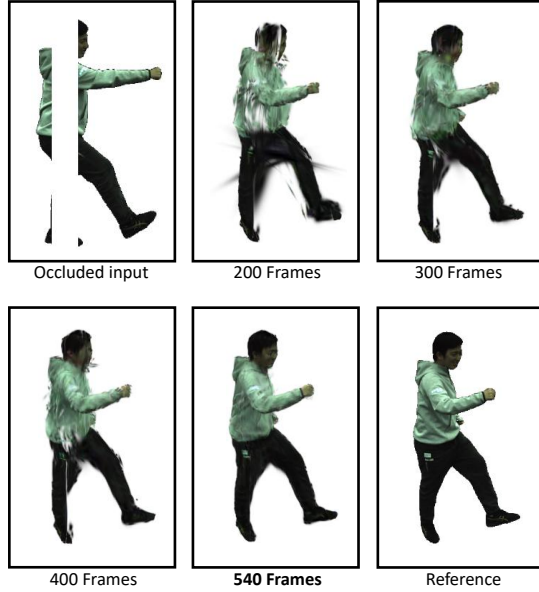


Figure 8. Qualitative results of ablation study on training frames.



Figure 9. The uneroded mask and eroded mask α_{body} .

find the optimal value of k . We performed this ablation experiment on subject 386 of the ZJU-MoCap dataset, and as shown in Table 4, the metrics are relatively superior when selecting $k=3$.

Table 4. Quantitative results of ablation study for K -nearest Occluded Points Query.

	PSNR \uparrow	SSIM \uparrow	LPIPS* \downarrow
k=1 nearest points	24.11	0.9544	39.36
k=3 nearest points	24.05	0.9536	39.75
k=5 nearest points	24.06	0.9538	39.12
k=8 nearest points	24.08	0.9541	39.27
k=10 nearest points	24.05	0.9542	39.38

A.6 More Qualitative Results on ZJU-MoCap and OcMotion

Figure 10 shows more qualitative rendering results of our OccGaussian and the SOTA method OccNeRF. It can be observed that compared to OccNeRF, our method does not produce unnecessary artifacts, exhibits better texture continuity in occluded regions, and yields more realistic rendering results.

A.7 Other Results based on 3DGS

We also employed other human body rendering methods based on 3D Gaussian Splatting to directly render the human under occlusions, demonstrating that our OccGaussian can efficiently render a more complete human body in the occluded scenes. We choose the 3DGS-Avatar [40] that utilizes 3D Gaussian Splatting to reconstruct clothed human avatars from monocular videos. The experiments on the ZJU-MoCap dataset are shown in Figure 11. It can be seen that our OccGaussian can render a complete human with high quality, filling appropriate textures in the occluded areas. Meanwhile, 3DGS-Avatar fails to render the human body under occlusion, leaving large blank areas without color in many regions.

A.8 Ablation Results for Training Frames

On subject 387 of the ZJU-MoCap dataset, we conduct an ablation study using different number of training frames. As shown in Figure 8 and Table 5, training with more frames improves the rendering quality of the model. Training with 200 frames does not result in a complete human silhouette and renders a lot of artifacts. Training with 300 and 400 frames gives a more complete human body, but there are still some parts of the body that are fragmented and lose a lot of detail. Our 540-frame model better recovers the overall texture of the clothes and facial details, giving the most realistic rendering results.

Table 5. Quantitative results of ablation study for different training frames.

	PSNR \uparrow	SSIM \uparrow	LPIPS* \downarrow
200 frames	21.15	0.9279	61.04
300 frames	21.87	0.9367	49.44
400 frames	22.66	0.9418	44.35
540 frames	23.02	0.9422	44.47



Figure 10. More qualitative results between our OccGaussian and OccNeRF on ZJU-MoCap and OcMotion datasets.

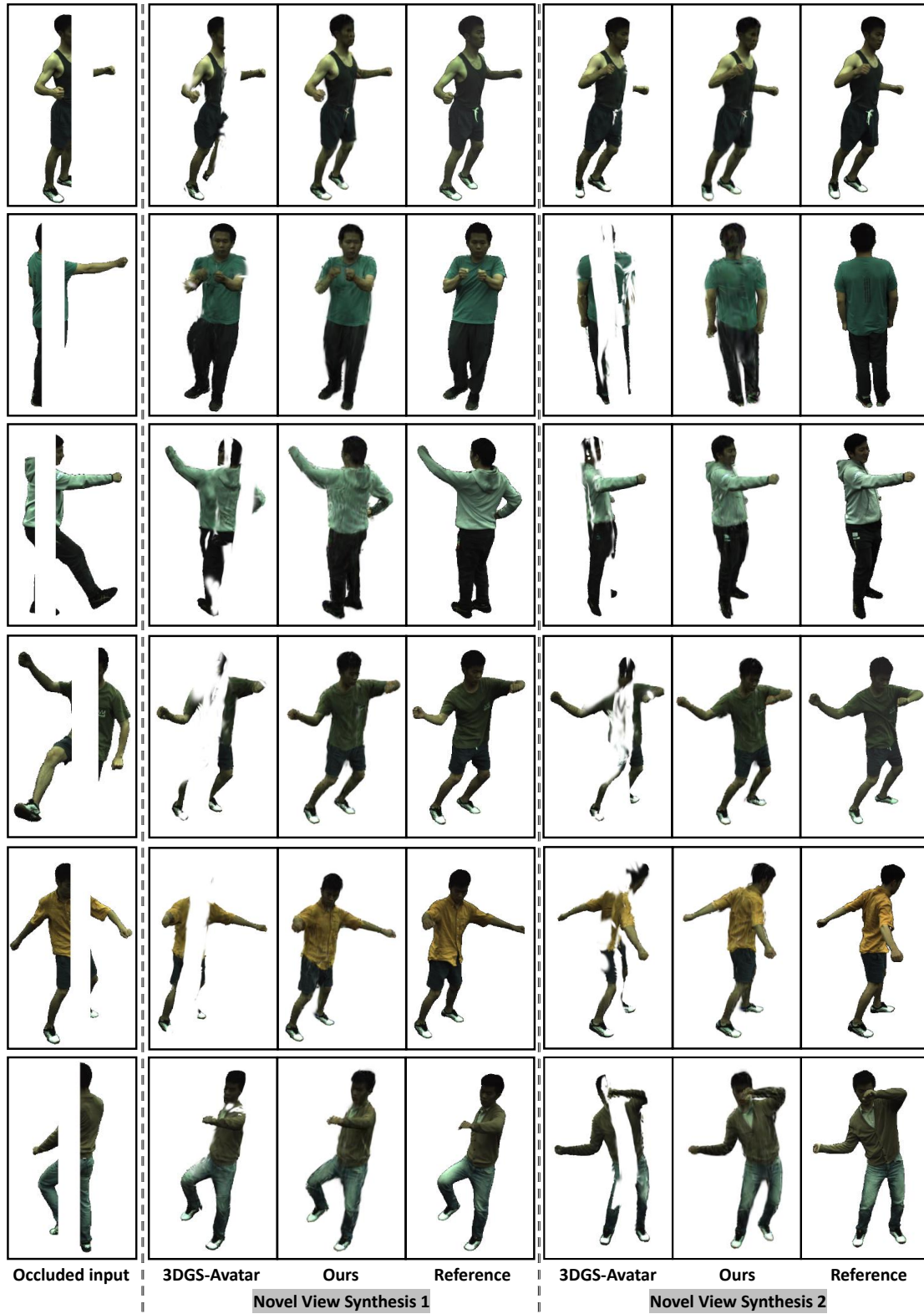


Figure 11. Qualitative results between our OccGaussian and 3DGS-Avatar on the ZJU-MoCap datasets.